SUBMISSION TO 'CANADIAN GEOTECHNICAL JOURNAL'

DATE:

28/10/2015

TITLE:

Improved image-based deformation measurement for geotechnical applications

AUTHORS:

S. A. Stanier[1], J. Blaber[2], W. A. Take[3] and D. J. White[4]

POSITIONS AND AFFILIATIONS:

[1] Research Fellow– UWA, Australia.
[2] Post-graduate Student – Georgia Tech, USA.
[3] Associate Professor – Queen's University, Canada.
[4] Professor – UWA, Australia.

CONTACT ADDRESS:

Dr. Sam Stanier
Centre for Offshore Foundation Systems
University of Western Australia
M053 Fairway
Crawley
WA 6009

NUMBER OF WORDS, FIGURES AND TABLES:

Words: 4417
Figures: 13
Tables: 1

KEYWORDS:

Image analysis, model tests, particle image velocimetry, digital image correlation

IMPROVED IMAGE-BASED DEFORMATION MEASUREMENT FOR GEOTECHNICAL APPLICATIONS

S. A. Stanier, J. Blaber, W. A. Take and D. J. White

ABSTRACT

This paper describes and benchmarks a new implementation of image-based deformation measurement for geotechnical applications. The updated approach combines a range of advances in image analysis algorithms and techniques best suited to geotechnical applications. Performance benchmarking of the new approach has used a series of artificial images subjected to prescribed spatially-varying displacement fields. An improvement by at least a factor of ten in measurement precision is achieved relative to the most commonly used particle image velocimetry (PIV) approach for all deformation modes, including rigid body displacements, rotations and strains (compressive and shear). Lastly, an example analysis of a centrifuge model test is used to demonstrate the capabilities of the new approach. The strain field generated by penetration of a flat footing and an entrapped sand plug into an underlying clay layer is computed and compared for both the current and updated algorithms. This analysis demonstrates that the enhanced measurement precision improves the clarity of the interpretation.

INTRODUCTION

Measurement of soil deformations in geotechnical models using Particle Image Velocimetry (PIV) techniques (Adrian 1991) – also known as Digital Image Correlation (DIC) (Sutton et al. 1983, Sutton et al. 2000) – has become routine experimental practice in many geotechnical research laboratories over the past fifteen years (White et al. 2001, White et al. 2003, Rechenmacher and Finno 2004, Iskander 2010, Hall 2012, Take 2015). The capabilities of the algorithms and analysis techniques that underpin PIV/DIC have also significantly improved over the same timeframe.

Figure 1(a) illustrates the typical setup of a geotechnical PIV/DIC analysis for a shallow footing experiment. A wide range of deformation levels are present and accurate and precise displacement data is desired in both the near- and far-field regions of the model. In a typical PIV/DIC analysis, a Region of Interest (RoI) is first defined within the initial ('reference') image of the model and populated with a mesh of subsets (or 'patches') of user-defined size. The displacements of these subsets in subsequent ('target') images are found using one of the approaches illustrated in Figure 1(b). Most freely available PIV/DIC software used for geotechnical analyses use some form of cross-correlation to obtain integer pixel displacements followed by sub-pixel interpolation of the correlation peak (e.g. GeoPIV (White et al. 2003); MatPIV (Sveen and Cowen, 2004; PIVlab (Thielicke and Stamhuis, 2014) and OpenPIV (Taylor et al. 2010)). In these algorithms the subsets (or 'patches') are generally not allowed to deform (so-called zero-order deformation).

More sophisticated PIV/DIC algorithms exist, and are introduced later in this paper. They incorporate higher-order subset shape functions (typically first-order, thus allowing displacement gradients across the subsets), image intensity interpolation and deformation parameter optimization, (e.g. Pan et al. 2006, 2012, Sutton et al. 2000). Some of these advances have been incorporated in commercially-available PIV/DIC software (e.g. Vic-2D

(Correlated Solutions, 2015); LaVision DaVis8 (LaVision, 2015); MI-2D (Match-ID (2015)) although these are not freely available to the academic community and the specific algorithms used are often proprietary. For applications in which small strains are of interest, such as geotechnical modeling and structural monitoring, photogrammetric corrections are often needed to obtain sufficiently accurate PIV/DIC results and these correction routines are not usually integrated within either freeware or commercial programs.

The purpose of this paper is to: (i) describe the advantages that the more sophisticated genera of PIV/DIC algorithms provide for geotechnical applications involving small and large deformations; and (ii) quantify these advantages via benchmark cases using a freely available non-commercial algorithm that is well-suited to the analysis of geotechnical model test images.

The specific software used for the benchmark cases is referred to as GeoPIV-RG and is an update of the GeoPIV program (which represents the typical algorithms currently used in research, and is described by White et al. (2003)). A brief overview of the computational approach is first given. The comparison is then performed using artificial 'soil-like' images subjected to various modes of deformation. Lastly, an example application is given that illustrates the impact this improvement in measurement precision can have on the interpretation of a classical geotechnical problem.

COMPUTATIONAL METHOD

Digital images captured during a geotechnical model test are usually analysed in sequence, starting with an initial 'reference' image. If the 'reference' image is retained as the initial image (the so-called 'leapfrog' scheme; see Figure 2(a)) then zero-order subsets can suffer a loss of correlation in regions experiencing large deformations (Figure 2(d)) due to a mismatch between the subset shape and the deformation being observed. Alternatively, if the 'reference' image is updated after every computation (the so-called 'sequential' scheme; see Figure 2(b))

so as to minimize the distortion that would reduce the correlation in the 'target' images, random walk errors are accumulated (White et al. 2003) because the overall displacement is being found as the sum of many small displacements, each of which have an associated error (Figure 2(d)). Random walk errors can become significant in regions of low deformation when calculating strains from the derivatives of displacement.

The current version of GeoPIV uses a combination of these two schemes to minimise accumulated random walk errors whilst maintaining tolerable correlations. The number of increments to be performed using the 'leapfrog' scheme prior to updating the 'reference' image (the so-called 'leapfrog' parameter) is manually defined by the user by trial and error guided by the amount of deformation occurring between sequential images. Also, the 'search zone' over which the correlation measure is computed for each subset (s_{zone}) is specified by the user in GeoPIV. Unnecessarily large values of s_{zone} lead to computational inefficiency in regions of images experiencing small displacements so small values are preferred. However, the value specified must be larger than the maximum displacement expected to occur between the 'reference' and 'target' images (see Figure 2(a,b)). Therefore, s_{zone} also cannot be predetermined and requires further trial-and-error refinement to achieve the best balance between accuracy and computational efficiency.

The new implementation presented in this paper avoids the need for trial-and-error refinement of either the 'leapfrog' value or the 'search zone' parameter by following the process illustrated in Figure 2(c) for each subset. The overarching framework controlling the computation process is the Reliability-Guided (RG) method proposed by Pan (2009), as implemented in Matlab by Blaber et al. (2015) (so the software is referred to as GeoPIV-RG). Each 'reference' subset is allowed to deform using a shape (or warp) function describing first-order deformations in conjunction with image intensity interpolation techniques to improve the correlation between 'reference' and 'target' subsets via optimisation (Schreier and Sutton 2002). After an initial 'seed' subset has been analysed, subsequent computations are

preconditioned using the results from the previously computed neighbouring subset that has the highest correlation (the so-called 'preconditioned optimisation' scheme; see Figure 2(c)). This approach leads to the definition of a 'search zone' being unnecessary whilst allowing the effective 'search zone' to be the whole image if necessary should the preconditioning process not yield a close match to the optimised solution for any particular subset. The 'reference' image is updated when the correlation coefficient for either the seed or one of the subsets contravenes user-defined thresholds, effectively optimising the 'leapfrog' parameter. The first-order subset shape function (which allows for linear gradients of displacement across the subset) leads to improved precision and reduced random walk errors (see Figure 2(d)) because correlation is better preserved allowing the 'reference' image to be updated less frequently for image sequences experiencing low deformations. The overall programmatic structure of the implementation is summarised by the flowchart in Figure 3.

Seed Computation

The computation process begins at a selected subset (circular in shape in this instance) from part of the RoI that experiences minimal deformation, meaning that the correlation between the 'reference' and 'target' subset will be high and thus the chances of an incorrectly computed seed occurring will be low. This point is used as a 'seed' from which the RG computation process propagates. The displacement of this subset is computed following the procedure outlined in Figure 4(a). Initially, the displacement of the seed subset is estimated to the nearest integer pixel value using Normalised Cross Correlation (NCC) (Lewis, 1995). Next the subset is allowed to deform using a subset shape function (p) that describes a superposition of the first order subset deformation modes illustrated in Figure 5 (Pan et al. 2006). The Inverse Compositional Gauss-Newton (IC-GN) method described by Pan et al. (2013) is used, in combination with bi-quintic B-spline interpolation of the deformed subset pixel intensities (e.g. Cheng et al. 2002) to adjust the subset shape function until the correlation between the 'reference' and 'target' subsets is optimised. The exit criterion for the

optimisation is a user-defined maximum magnitude for the norm of the subset shape function difference vector ($|\Delta p|_{max}$) between successive computations (typically 1×10^{-5}) and a maximum number of iterations (max_{iter}) per subset (typically 50). The zero-normalised cross-correlation correlation coefficient (CC_{ZNCC}) is used to indicate the degree of match where values of 1, 0 and -1 indicate perfect, zero and inverse correlations respectively (Pan et al. 2010). The seed computation is deemed successful if the CC_{ZNCC} is greater than a user-defined limit, $CC_{ZNCC\text{-}seed\text{-}tol}$ (typically 0.9).

Reliability-Guided Computations

Assuming the 'seed' computation was successful, a high-density grid of subsets is processed using the RG framework outlined in Figure 4(b). Firstly the CC_{ZNCC} of the four subsets surrounding the seed are estimated using the displacement and deformation parameters for the seed subset as an initial estimate (Zhou and Chen, 2012). These four subsets are then placed in a queue of descending CC_{ZNCC} from which the subset with the optimal correlation coefficient is selected first. IC-GN and bi-quintic B-spline interpolation is once again used to optimise the deformation parameters for this subset, then it is removed from the queue. If not already in the queue, the CC_{ZNCC} is computed for the neighboring subsets and those subsets are added to the queue. This process repeats, calculating the displacement and deformation of all of the subsets across the entire RoI. The advantage of the RG framework over the usual processing of subsets across successive rows is three-fold: firstly, the NCC, which is computationally expensive to determine, is only computed for the seed subset and covers the entire region of interest. Secondly, the subsets with higher correlation coefficient are processed first, and the optimised deformation parameters used to precondition the IC-GN optimisation of the neighbouring subsets. Thirdly, as a result of this approach, the need to specify the expected maximum displacement within the displacement field is eliminated.

Reference Image Updating

Compared to conventional PIV/DIC applications, geotechnical model testing can involve tracking of a larger range of deformations and highly circuitous displacement paths. For example soil often flows around penetrometers and deeply buried foundations. Unlike fluid mechanics studies, where constitutive relations are not a focus, geotechnical research is concerned with both instantaneous flow fields and also the strain path histories, stress-strain behaviour and the associated constitutive relations. Additional measures are therefore required to handle the resulting changes in subset appearance, for example due to grain rearrangement, because these lead to a reduction in the subset correlation and cause erroneous displacements to be estimated (known as 'wild' vectors). To counter this degradation of correlation the 'reference' image can be periodically updated. In earlier versions of GeoPIV the updating interval was specified manually by the user and refined through trial and error (White et al. 2003). An automatic 'reference' image-updating scheme, similar to that proposed by Pan et al. (2012), is used in GeoPIV-RG. After completion of the RG computations for each target image the CC_{ZNCC} for each subset is compared to a second, slightly relaxed, user-defined limit (typically 0.75) denoted $CC_{ZNCC\text{-}min\text{-}tol}$. Using a relaxed tolerance on the minimum permissible full field CC_{ZNCC} allows large deformations to occur in certain regions of the model prior to 'reference' image updating. If the CC_{ZNCC} for any subset is less than $CC_{ZNCC\text{-}min\text{-}tol}$ then the 'reference' image is updated to the target image from the last successful increment, otherwise the current 'reference' image is carried forward.

The RG method is programmed to compute the displacement of regularly gridded subsets. Consequently, an interpolation scheme is required to compute the displacement of the user-defined subset locations from the regularly gridded RG output. Bi-cubic spline interpolation of the output from the RG process achieves this. To safeguard the precision of the measurements during the interpolation process, the subset spacing used in the RG process is reduced relative to that given in the user-defined mesh. For the benchmarking analyses

presented in this paper halving the grid spacing was sufficient to preserve accuracy of the measurements. Due to the computational efficiency of the preconditioned IC-GN optimisation process, the computational cost of this four-fold increase in RG computation grid density is minimal. The 'reference' image updating procedure ensures that the updating interval is always optimised. The user can control the frequency of 'reference' image updating indirectly by varying the correlation coefficient tolerances, $CC_{ZNCC\text{-}seed\text{-}tol}$ and $CC_{ZNCC\text{-}min\text{-}tol}$, with stricter values resulting in more frequent 'reference' image updating.

PERFORMANCE COMPARISON

Methodology

The performance of GeoPIV-RG is compared to GeoPIV (described by White et al. 2003 and White et al. 2005), which is widely used in geotechnical research and is typical of the many freely available zero-order algorithms (e.g. MatPIV, PIVlab and OpenPIV). Therefore the following benchmarking analyses are generally indicative of the improvements in measurement precision that can be attained by incorporating advances in PIV/DIC including first-order subset shape functions, image intensity interpolation, deformation parameter optimisation and automatic 'reference' image updating schemes similar to those described earlier.

Artificial images that represent geomaterials are preferred for such benchmarking as they can be subjected to precisely prescribed deformations and are unaffected by camera-induced lens distortions and camera-target movements (Lee et al. 2012). The images were generated in Matlab by randomly projecting thousands of white dots onto a black background to sub-pixel positional resolution. Each white dot is defined by a Gaussian brightness peak centered at a specified location. In this way the location of the dot can be precisely controlled allowing smooth spatially-varying displacement fields to be prescribed. The 'reference' artificial image used in all of the artificial benchmarking analyses presented herein is shown in Figure 6(a)

with the 1681 subset locations marked by yellow crosses in a centrally located zone, of 400 × 400 pixels. This subset population is sufficiently large to generate statistically valid measurements of the error in the image-based displacement measurements. For GeoPIV the side length of the square subsets, L_s, was 45 pixels, while for GeoPIV-RG the subset diameter, D_s, was taken as 50 pixels giving comparable total pixels per subset (within ~3%).

The theoretical and measured displacements at the 1681 subset locations were compared for four deformation modes: (i) rigid body translation, (ii) rigid body rotation, (iii) vertical strain and (iv) pure shear strain as illustrated in Figure 6 (b-e). For rigid body translation, displacement was applied in 0.025 pixel increments up to a maximum of 1 pixel. For the rotation, vertical strain and pure shear strain analyses the deformation magnitude imposed was increased over 100 logarithmically spaced intervals up to a maximum of 90° of rotation and 50% strain. The total deformation applied was chosen such that 'reference' image updating was periodically required so the efficacy of the full computational scheme has been validated. For the analyses performed using the current version of GeoPIV the 'reference' image was updated manually as infrequently as possible to minimise the summation of random walk errors.

The precision error in the displacement measurements is quantified by the standard error, ρ_{px}, defined as the standard deviation of the difference between the theoretical and calculated subset displacement over the 1681 subsets. It is shown later that this error increases as the deformation of the subset increases. To convert these standard errors to a measure of the precision with which deformations can be determined, the measurement errors (δ) are defined as the error in the measured deformation, for a given level of that deformation mode. An estimate of the random error δ for each mode (rotation, vertical strain and pure shear strain) can then be defined as:

$$\delta_\theta = \tan^{-1}\left(\frac{\sqrt{2}\rho_{px}}{L}\right) \quad (1)$$

$$\delta_{\varepsilon_y} = \frac{\sqrt{2}\rho_{px}}{L} \quad (2)$$

$$\delta_{\varepsilon_{xy}} = \frac{\sqrt{2}\rho_{px}}{L} \quad (3)$$

where θ, ε_y and ε_{xy}, denote rotation in degrees, vertical strain and pure shear strain respectively and L is a nominal gauge length in pixels. Each random error δ is estimated for L = 25, 250 and 2500 pixels, which cover the range typically relevant. When viewing a geotechnical model test, the varying deformation throughout the image is of interest, so the relevant gauge length is comparable to the spacing of the subsets, i.e. of the order of 25 pixels. Alternatively, when viewing a geotechnical element test, at a stage when the deformation is uniform, the gauge length might be significantly larger, i.e. of the order of 2500 pixels. The δ estimates, combined with a tolerable measurement error, allow the required subset spacing to be identified. Alternatively, they show the image scale (e.g. pixels/mm) required in a model test to detect a specific level of deformation.

Results

Rigid body translation

The standard errors, ρ_{px}, in Figure 7(a) are ~0.005 and ~0.0008 pixels for GeoPIV and GeoPIV-RG respectively, indicating a modest improvement in precision for sub-pixel displacement measurement for the new methods. Meanwhile, Figure 7(b) presents the mean bias error, μ_{bias} (Schreier et al. 2000), which is the mean discrepancy between the actual and measured displacement, for the sub-pixel rigid body translation analysis. For GeoPIV, which uses NCC to obtain the integer pixel displacements prior to sub-pixel interpolation using bi-cubic splines, a significant periodic variation in μ_{bias} is evident for non-integer or non-half-

integer displacements. This behaviour is consistent with that reported by Amiot et al. (2013) for PIV/DIC software incorporating bi-cubic interpolation. In contrast, the bi-quintic B-spline interpolation process used in the IC-GN optimisation of GeoPIV-RG suffers from mean bias errors that never exceed 0.0005 pixels. This is comparable to the performance reported by Lee et al. (2012) for NCC with bi-quintic B-spline sub-pixel interpolation and consistent with the best performing PIV/DIC software (w.r.t. mean bias errors) reported by Amiot et al. (2013) that also incorporated bi-quintic b-spline interpolation. Minimising bias errors is particularly important if strains are to be derived from the derivatives of displacement fields. Periodic bias can lead to erroneous localizations in strain fields if periodic bias errors are evident.

Rigid body rotation

Figure 8(a) shows the evolution of ρ_{px} with rigid body rotation. GeoPIV accumulates significant errors with increasing rotation because the ability of NCC to accurately track subset displacements progressively degrades with rotation (Dutton et al. 2014), causing accumulating drift in the displacements. The iterative subset deformation optimisation performed by GeoPIV-RG mitigates the degradation of correlation, resulting in a comparatively small precision error of $\rho_{px} < 1/1000^{th}$ of a pixel, irrespective of the rotation magnitude, whilst the mean errors are always less than 1×10^{-4} pixels. As a result, the rotation error, δ_θ, is approximately constant for rotation magnitudes greater than 1° (Figure 8(b)).

The divergence in performance between GeoPIV and GeoPIV-RG observed in Figure 8 has a profound effect on the abilities of the respective algorithms to measure strain fields because the magnitude of the error is random and not linked to the magnitude of the displacement of the subset. To illustrate this an additional analysis was performed using the same analysis parameters and artificial images for a horizontal row of subsets spaced at 1-pixel intervals at increasing distance from the origin of rotation (L_o) up to a maximum of 200-pixels. For these subsets and for all rotation increments, the rotation angle is the same but the displacement

magnitude increases proportionally with the distance from the origin of rotation, as illustrated in Figure 9(a). The resultant error magnitudes (δ_r) were calculated for rotation angles of 0.0°, 0.5°, 1.0°, 1.5° and 2.0° and are plotted with respect to the distance from the origin of rotation in Figure 9(b) and (d) for GeoPIV and GeoPIV-RG respectively.

From these results it is clear that the error magnitudes and directions are random and unrelated to the distance from the origin of rotation. However, the error magnitudes are clearly linked to the rotation angle as the error magnitude tends to increase with rotation angle, as is confirmed for GeoPIV in Figure 9(c) and GeoPIV-RG Figure 9(e) where the evolution of errors are presented with respect to the rotation angle imposed for subsets located at sections A–A, B–B and C–C.

For a basic PIV/DIC analysis where vector plots are used to illustrate soil flow mechanisms the poor performance of GeoPIV for rotation is not necessarily problematic as the large magnitude of the vectors within the soil flow mechanism will mask the errors induced by rotation. However, if strains are derived from the derivatives of the displacement components the errors become very significant. For example, for a strain element with length L=25px positioned either side of subset A–A, similarly to Equations 1-3, a generic estimate of the strain error (δ_ε) can be taken as follows:

$$\delta_\varepsilon = \frac{2|\delta_r|}{L} \tag{4}$$

For a rotation angle of 2°, the strain error for GeoPIV is of the order of ~3%, significantly limiting the ability to plot meaningful strain fields. On the other hand, the strain errors for GeoPIV-RG are less than ~0.03%, resulting in a two order of magnitude improvement in strain measurement resolution as a result of the additional degrees of freedom provided by the first order subset shape function. The impact of this improvement is significant for geotechnical research applications where more than simple instantaneous flow mechanisms

are to be observed, such as when gross element distortions are to be monitored through large rotations.

Vertical and shear strain

Figures 10(a) and 11(a) illustrate that measurement precision during deformation – either through vertical strain or shear strain – is similar to rotation (ρ_{px} ~1/1000th pixel) until ~0.01 or 1% strain, beyond which the precision error rises approximately linearly with strain.

When converted to δ estimates (Figures 10(b) and 11(b)), these results allow the practicality of detecting a given strain level to be assessed. For example, if a model test with a varying deformation is being viewed, then a subset spacing of typically 25 pixels might apply. In this case, if zones of the model have undergone strains of 1% or 10% (points M1 and M2 on Figures 10b and 11b), the resulting strain errors would be ~0.025% and ~0.25% respectively (equivalent to a signal-to-noise ratio, *SNR*, of ~40), which is likely to be adequate for producing detailed and smooth deformation fields (e.g. 20 contours of 0.05% or 0.5% up to the maximum of 1% or 10% respectively). Alternatively, if the application is an element test with uniform deformation, so the gauge length is a larger proportion of the image width – typically 2500 pixels in width – then at a strain of 0.1% (100 microstrain) the strain error is ~5×10^{-7} (point E on Figures 10(b) and 11(b)) or 0.05 microstrain (equivalent to a signal-to-noise ratio, *SNR*, of ~2000).

All of these artificial image analyses show that the new approach is at least an order of magnitude more precise than the combination of NCC and bi-cubic spline interpolation method employed by GeoPIV (White et al. 2003), for both small and large deformations.

EXAMPLE APPLICATION

To demonstrate the application of the new methodology, images from a model test performed in the drum centrifuge at UWA are used. The test involved similar techniques to the work

reported by Hu et al. (2014), investigating punch-through of a 30mm diameter flat footing (at 200*g*, so equivalent to 6m diameter at prototype scale) on a 20mm deep (4m prototype) sand layer overlying clay. In the experiment ~550 images were recorded at a frequency of 5Hz using the apparatus described by Stanier and White (2013). Artificial texture was applied to the exposed face of the model at the optimal Artificial Seeding Ratio (*ASR*) following the procedure proposed by Stanier and White (2013) to maximise the precision of the image-based deformation measurements.

Analyses were performed on the series of images for the underlying clay layer only, using both GeoPIV and GeoPIV-RG with the analysis settings summarised in Table 1. The time taken by each of the algorithms to perform an analysis is dependent upon a number of factors, including: the subset spacing, deformation magnitude, image texture quality and available processing power. For this particular analysis GeoPIV-RG performed the computations in ~20% of the time taken by GeoPIV. The total maximum shear strain ξ (i.e. $\Delta\varepsilon_1 - \Delta\varepsilon_2$ summed through the deformation) was calculated from the displacement fields following the large strain procedure of White and Bolton (2004).

Figure 12 presents the distributions of ξ after 1*D* of footing penetration. Significant noise is evident in the results from GeoPIV from summed random walk errors and degradation of correlation due to subset rotation and deformation. In contrast the analysis generated by GeoPIV-RG has lower noise, as is evident in the regions experiencing small strains. Figure 13 shows a horizontal cross section through both analyses at an initial normalised depth, *z*/*D* of 1.5, presented in terms of both the normalised displacement magnitude and total maximum shear strain. The first-order deformation algorithm of GeoPIV-RG results in smoother spatial variation of both the displacements and strains across the model, compared to the stepped cross-section resulting from the zero-order deformation algorithm of GeoPIV.

These enhancements result from the subset deformation optimisation capability of GeoPIV-RG as it preserves correlation and precision in regions of large deformation. The 'reference'

image also requires updating less frequently (see Table 1), which in turn minimises random walk errors. These advances create more precise deformation measurements, which unlocks additional potential applications. For example, more detailed verification of constitutive models by extracting element-level responses within model tests, and the quantification of geomaterial behavior at both smaller strains and higher levels of rotation and deformation than was possible using previous image analysis methods.

CONCLUSIONS

This paper has shown that recent advances in PIV/DIC algorithms coupled with photogrammetric correction routines allow improved deformation measurements for geotechnical applications. The algorithms have been incorporated in an update of a commonly-used freeware PIV/DIC program. The prior version has been used as a benchmark representing the approaches commonly used in geotechnical physical modelling. The benchmarking used a series of artificial soil-like images subjected to prescribed displacements and deformations. The advanced algorithms are faster and more precise than the simpler zero-order PIV/DIC approach that is widely used and freely available to the research community. Rigid-body displacements can be detected to a precision of ~0.001 pixels. There is a modest reduction in precision when the tracked soil is deforming. The effect of the gauge length (i.e. the separation of the measurement points) and the level of deformation or rotation on the precision of deformation measurements is quantified. For example, it is shown that when soil elements at close spacing experience rotation in a model test, the new implementation is approximately two orders of magnitude more precise than the existing approach, resulting in significantly less noise in strain fields derived from the derivatives of the displacements. At the other end of the scale, in an element test in which digital images are used to monitor the overall response of the sample (i.e. the gauge length is significantly larger and taken here as 2500 pixels), the standard error is ~0.05 microstrain at a strain of 0.1%.

An example analysis illustrates the value of the new approach by showing improved measurement of deformations during punch-through of a flat footing on a sand-over-clay stratigraphy. These results demonstrate the benefits of the enhanced measurement precision provided by this software, which is freely available to the geotechnical research community.

ACKNOWLEDGEMENTS AND SUPPLEMENTARY DATA

The research presented here forms part of the activities of the Centre for Offshore Foundation Systems (COFS), currently supported as a node of the Australian Research Council Centre of Excellence for Geotechnical Science and Engineering (grant CE110001009) and through the Fugro Chair in Geotechnics, the Lloyd's Register Foundation Chair and Centre of Excellence in Offshore Foundations and the Shell EMI Chair in Offshore Engineering (held by the fourth author). The third author is supported by the Natural Sciences and Engineering Research Council of Canada (NSERC) and holds a Canada Research Chair at the GeoEngineering-Centre at Queen's-RMC. The software code and example images relevant to this paper can be downloaded from www.geopivrg.com.

NOMENCLATURE

ASR	artificial seeding ratio
CC_{ZNCC}	zero normalised cross-correlation correlation coefficient
$CC_{ZNCC\text{-}min\text{-}tol}$	full field correlation coefficient tolerance
$CC_{ZNCC\text{-}seed\text{-}tol}$	seed correlation coefficient tolerance
d	displacement
δ_{ε}	strain error
$\delta_{\varepsilon_{xy}}$	shear strain error
$\delta_{\varepsilon_{y}}$	vertical strain error
δ_r	resultant error
δ_θ	rotation error
D	diameter
D_s	diameter of GeoPIV-RG subset
ε_1	major principal strain
ε_2	minor principal strain
ε_{xy}	pure shear strain
ε_y	vertical strain
L	gauge length
L_s	length of GeoPIV subset
max_{iter}	maximum number of iterations per subset
NCC	normalised cross correlation
p	subset deformation shape function
$\|\Delta p\|_{max}$	maximum norm of the shape function difference vector
px	pixel
ρ	undrained shear strength gradient

ρ_{px}	standard error of displacement measurement in pixels
r	radius
RoI	region of interest
s	subset spacing
SNR	signal-to-noise-ratio
s_{zone}	search zone parameter
u	horizontal displacement
v	vertical displacement
x	horizontal position
x_f	final horizontal position
x_i	initial horizontal position
y	vertical position
y_f	final vertical position
y_i	initial vertical position
z	depth
$ZNCC$	zero normalised cross correlation
ξ	total maximum shear strain

REFERENCES

Adrian, R. J. 1991. Particle imaging techniques for experimental fluid mechanics. Ann. Rev. Fluid Mech. 23, 261–304.

Amiot, F., Bornert, P., Dupre, J-C., Fazzini, M., Orteu, J-J., Poilâne, C., Robert, L., Rotinat, R., Toussaint, E., Wattrisse, B. and Wienin, J.S. 2013. Assessment of digital image correlation measurement accuracy in the ultimate error regime: main results of a collaborative benchmark. Strain, 49: 283-496.

Blaber, J., Adair, B. and Antoniou, A. 2015. Ncorr: open-source 2D digital image correlation Matlab software. Experimental mechanics, doi: 10.1007/s11340-015-0009-1.

Cheng, P., Sutton, M.A., Schreier, H.W. and McNeill, S.R. 2002. Full field speckle pattern image correlation with B-spline deformation function. Experimental Mechanics, 42(3): 344-352.

Correlated Solutions 2015. The Vic-2D System: technology overview. http://www.correlatedsolutions.com/vic-2d/

Dutton, M., Take, W.A. and Hoult, N.A. 2014. Curvature monitoring of beams using digital image correlation. Journal of Bridge Engineering, 19, 05013001: 1-13.

Hall, S. 2012. Digital Image Correlation in Experimental Geomechanics. ALERT Geomaterials Doctoral Summer School 2012. ALERT Geomaterials. ISBN: 978-3-00-039683-0. pp. 69-102.

Hu, P., Stanier, S.A., Cassidy, M.J. and Wang, D. 2014. Predicting the peak resistance of a spudcan penetrating sand overlying clay. Journal of Geotechnical and Geoenvironmental Engineering, 140(2): 04013009.

Iskander M. 2010 Modelling in transparent soils. Springer. ISBN-13: 978-3642025006.

LaVision 2015. Digital Image Correlation. http://www.lavision.de/en/techniques/digital-image-correlation.php

Lewis, J.P. 1995. Fast normalized cross-correlation. Industrial Light and Magic. [Self-published, expanded and corrected version of: Lewis J.P. (1995) Fast Template Matching. Vision Interface 95, Canadian Image Processing and Pattern Recognition Society, Quebec City, Canada, May 15-19, 1995, p. 120-123].

Lee, C., Take, W.A. and Hoult, N.A. 2012. Optimum accuracy of two-dimensional strain measurements using digital image correlation. Journal of Computing in Civil Engineering, 26: 795-803.

Match-ID 2015. 2D and stereo digital image correlation platform. http://www.matchidmbc.be/

Pan, B. 2009. Reliability guided digital image correlation for image deformation measurement. Applied Optics, 48(8): 1535-1542.

Pan, B., Li, K. and Tong, W. 2013. Fast, robust and accurate digital image correlation calculation without redundant computations. Experimental mechanics, 53:1277-1289.

Pan, B., Wu, D. and Xia, Y. 2012. Incremental calculation for large deformation measurement using reliability-guided digital image correlation. Optics and Lasers in Engineering, 50: 586-592.

Pan, B., Xie, H. and Wang, Z. 2010. Equivalence of digital image correlation criteria for pattern matching. Applied Optics, 49(28): 5501-5509.

Pan, B., Xie, H., Xu, B., Dai, F. 2006. Performance of sub-pixel registration algorithms in digital image correlation. Measurement Science and Technology, 17:1615-1621.

Rechenmacher, A.L. and R.J. Finno 2004. Digital image correlation to evaluate shear banding in dilative sands. ASTM Geotechnical Testing Journal, 27 (1), 13-22.

Schreier, H.W., Braasch, J.R. and Sutton, M.A. 2000. Systematic errors in digital image correlation caused by intensity interpolation. Optical Engineering, 39(11): 2915–2921.

Schreier, H.W. and Sutton, M.A. 2002. Systematic errors in digital image correlation due to under matched subset shape functions. Experimental Mechanics, 42(3): 303-310.

Stanier, S. A. and White D. J. 2013. Improved image-based deformation measurement in the centrifuge environment. Geotechnical Testing Journal, 36(6): 1-14.

Sutton, M.A., McNeill, S.R., Helm, J.D., and Chao, Y. J. 2000. Advances in two-dimensional and three-dimensional computer vision. Photomechanics, Topics in Applied Physics, Vol. 77, pp. 323–372.

Sutton, M. A., Wolters, W. J., Peters, W. H., Ranson, W. F., and McNeill, S. F. 1983. "Determination of displacements using an improved digital correlation method." Image and Vision Computing, 1(3), 133–139.

Sveen, J.K and Cowen, E.A. 2004. Quantitative imaging techniques and their application to wavy flow. In J. Grue, P. L. F. Liu, and G. K. Pedersen, editors, PIV and Water Waves, World Scientific, 2004.

Take, W.A. 2015. Thirty-Sixth Canadian Geotechnical Colloquium: Advances in Visualization of Geotechnical Processes through Digital Image Correlation. Canadian Geotechnical Journal, doi: 10.1139/cgj-2014-0080.

Taylor, Z.J.; Gurka, R.; Kopp, G.A.; Liberzon, A. 2010. Long-Duration Time-Resolved PIV to study unsteady aerodynamics, IEEE Transactions on Instrumentation and Measurement, 59(12): 3262-3269, doi: 10.1109/TIM.2010.2047149.

Thielicke, W and Stamhuis, E.J. 2014. PIVlab – Towards user-friendly, affordable and accurate Digital Particle Image Velocimetry in MATLAB. Journal of Open Research Software 2(1):e30, doi: http://dx.doi.org/10.5334/jors.bl.

White D. J., Take W.A, Bolton M.D. & Munachen S.E. 2001 A deformation measuring system for geotechnical testing based on digital imaging, close-range photogrammetry, and PIV image analysis. Proc. 15th Int. Conf. on Soil Mech. and Geotech. Engng. Istanbul, Turkey. pp 539-542. pub. Balkema, Rotterdam

White, D. J., Take, W., and Bolton, M., 2003. Soil Deformation measurement using Particle Image Velocimetry (PIV) and photogrammetry, Géotechnique, 53(7): 619–631.

White D.J., Take W.A. and Bolton M.D. 2005. Discussion on: Accuracy of Digital Image Correlation for measuring deformations in transparent media. Sadek S., Iskander M.G., and Liu J., ASCE J. Computing in Civil Engineering. 19(2):217-219

White, D.J. and Bolton, M.D. 2004. Displacement and strain paths during plane-strain model pile installation in sand. Géotechnique, 54(6): 375-397.

Zhou, Y. and Chen, Y.Q. 2012. Propagation function for accurate initialization and efficiency enhancement of digital image correlation. Optics and Lasers in Engineering, 50(12): 1789-1797.

FIGURE CAPTIONS

Figure 1: PIV/DIC analysis overview: (a) typical PIV/DIC scenario with associated causes of error, (b) general overview of the PIV/DIC method.

Figure 2: Overview of (a) 'leapfrog', (b)'sequential', and (c) 'preconditioned optimisation' computation schemes alongside (d) schematic plots of the expected evolution of correlation coefficient and random walk errors.

Figure 3: Flowchart for GeoPIV-RG computations.

Figure 4: Flowcharts for seed subset (a) and RG subset computation sub-routines (b).

Figure 5: Subset deformation modes considered by the first-order shape function *p*: (a, b) displacements and (c-f) displacement gradients. Note: subsets are represented as squares for clarity but subset shape is arbitrary.

Figure 6: Artificial images and imposed deformations: (a) example image and subset locations (b) rigid body translation (c) rigid body rotation (d) vertical strain (e) pure shear strain.

Figure 7: Rigid-body translation performance: (a) standard error, ρ_{px}, and (b) mean bias error, μ_{bias}, for GeoPIV and GeoPIV-RG.

Figure 8: Rotation performance: (a) standard error for GeoPIV and GeoPIV-RG (b) effect of gauge length on rotation error, δ_θ, for GeoPIV-RG.

Figure 9: Randomness of rotation performance: (a) artificial image and a row of subset displacements (magnitudes amplified) illustrating the rotation imposed; (b,c) resultant error, δ_r, as a function of distance from the origin of rotation and rotation angle for GeoPIV; and (d,e) GeoPIV-RG. Note: Vertical scales are different between (a,b) and (c,d) for clarity.

Figure 10: Vertical strain performance: (a) standard error for GeoPIV and GeoPIV-RG (b) effect of gauge length on vertical strain error, δ_{ε_y}, for GeoPIV-RG.

Figure 11: Shear strain performance: (a) standard error for GeoPIV and GeoPIV-RG (b) effect of gauge length on shear strain error, $\delta_{\varepsilon_{xy}}$, for GeoPIV-RG.

Figure 12: Example application: flat footing on sand-over-clay, total maximum shear strain ζ at 1*D* penetration using GeoPIV (a) and GeoPIV-RG (b).

Figure 13: Normalised displacement, *δ*/*D* (a) and total maximum shear strain, ζ (b) along the cross-sections in Figures 12 (a, b) at an initial normalised depth, *z*/*D* of 1.5.

FIGURES

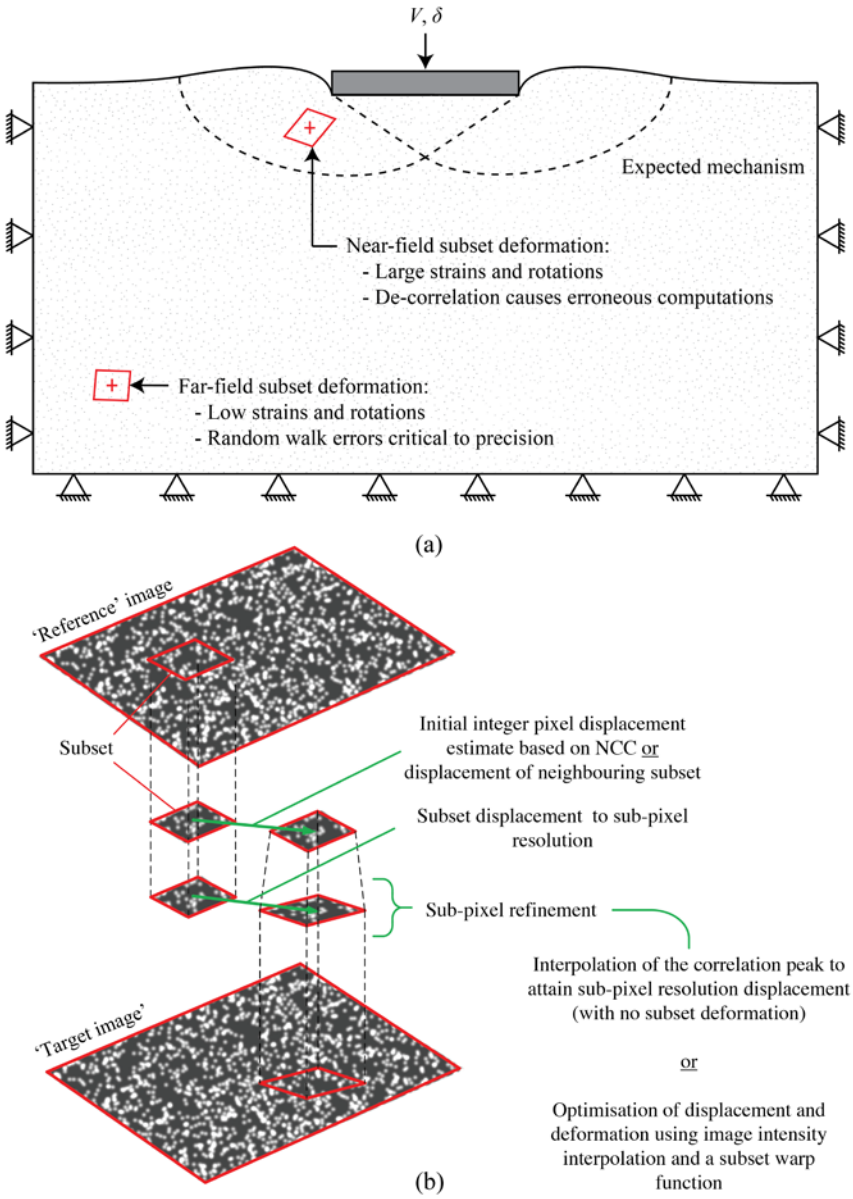

Figure 1: PIV/DIC analysis overview: (a) typical PIV/DIC scenario with associated causes of error, (b) general overview of the PIV/DIC method.

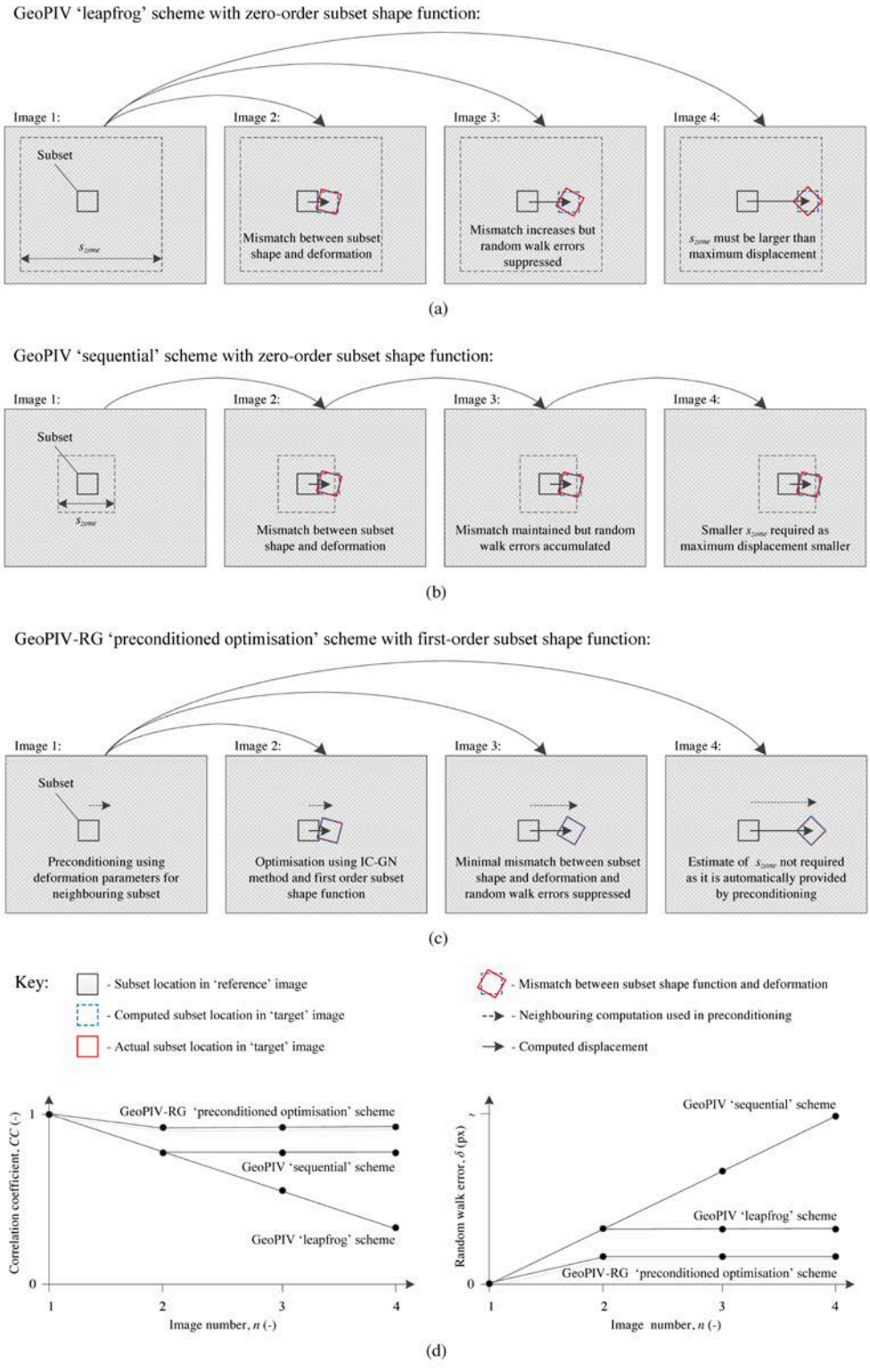

Figure 2: Overview of (a) 'leapfrog', (b)'sequential', and (c) 'preconditioned optimisation' computation schemes alongside (d) schematic plots of the expected evolution of correlation coefficient and random walk errors.

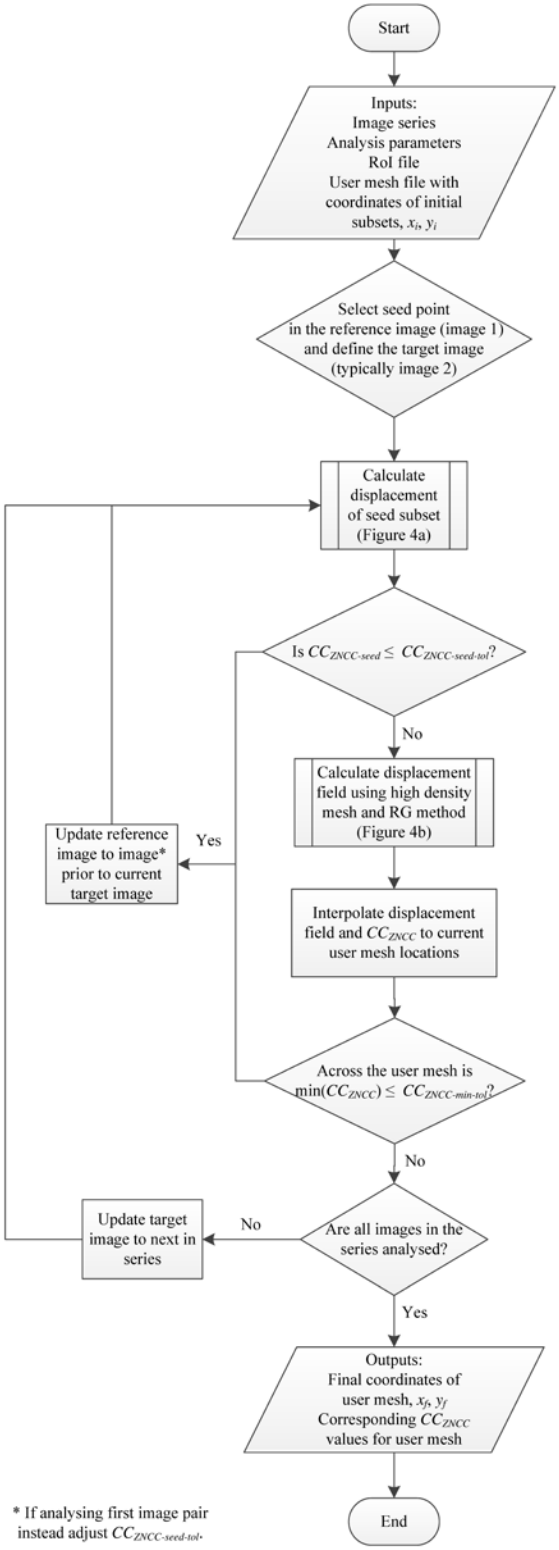

Figure 3: Flowchart for GeoPIV-RG computations.

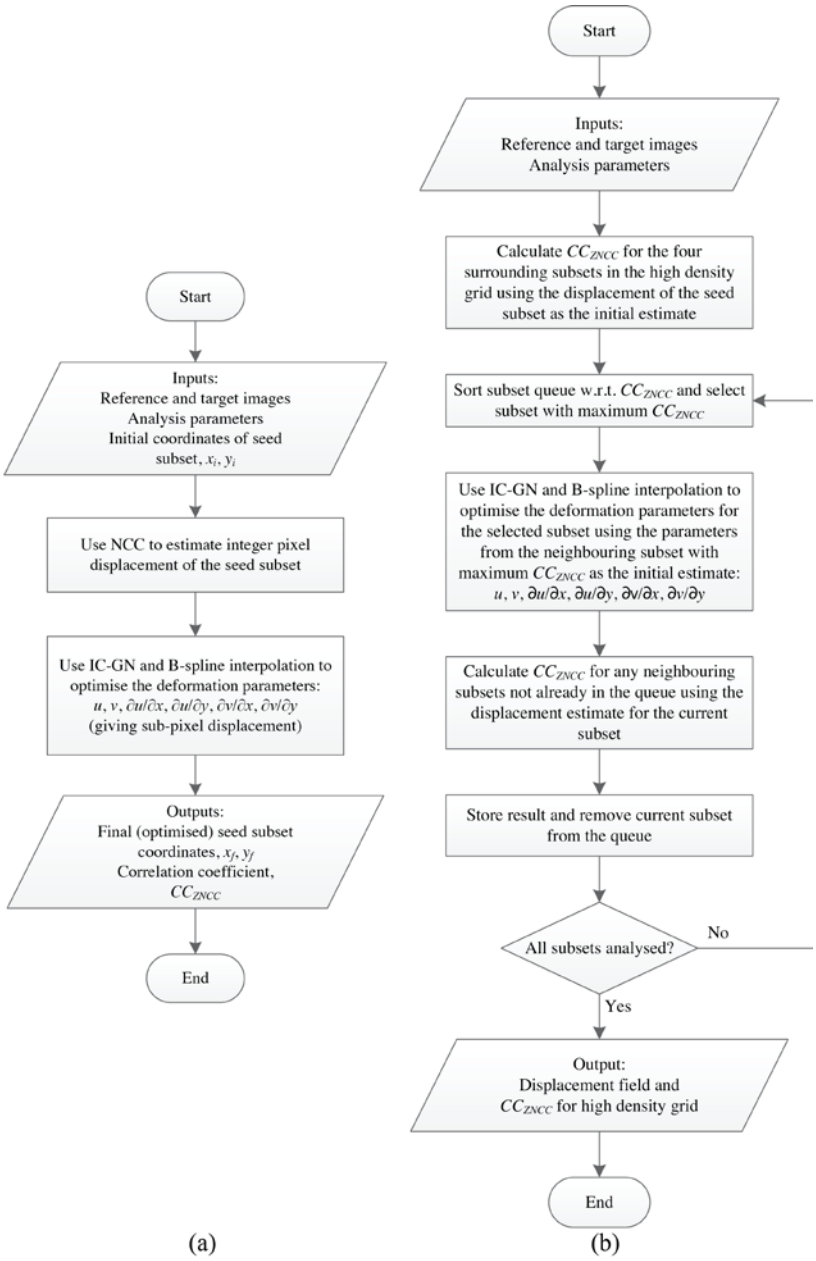

Figure 4: Flowcharts for seed subset (a) and RG subset computation sub-routines (b).

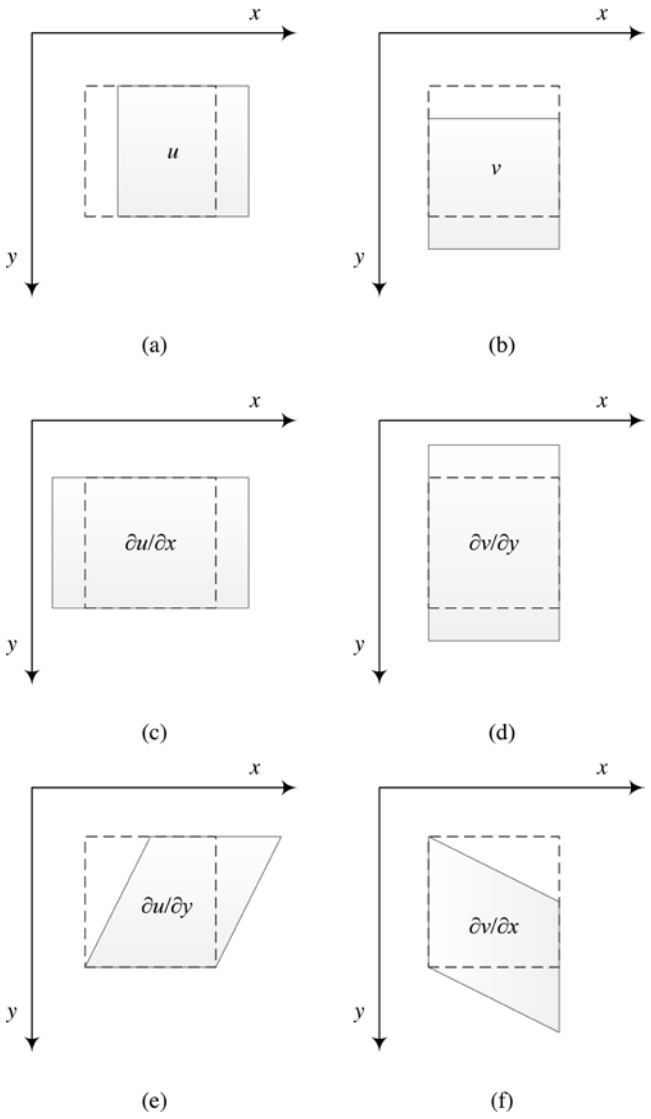

Figure 5: Subset deformation modes considered by the first-order shape function *p*: (a, b) displacements and (c-f) displacement gradients. Note: subsets are represented as squares for clarity but subset shape is arbitrary.

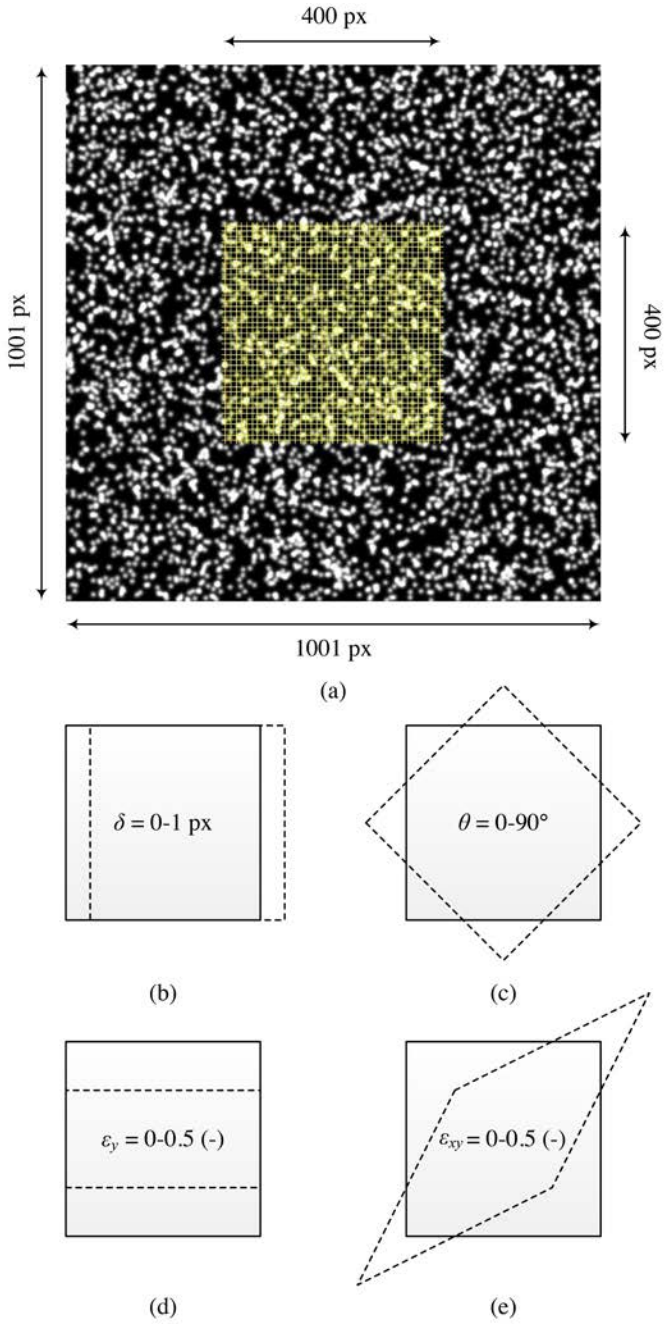

Figure 6: Artificial images and imposed deformations: (a) example image and subset locations (b) rigid body translation (c) rigid body rotation (d) vertical strain (e) pure shear strain.

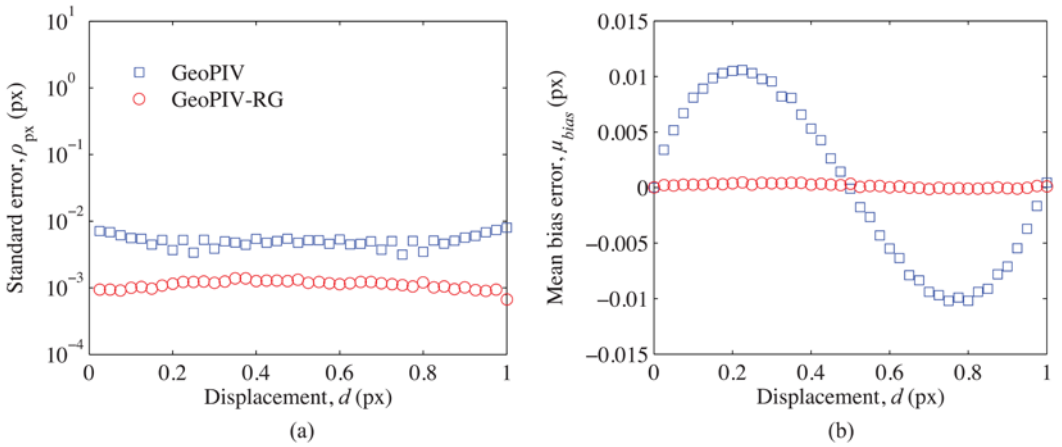

Figure 7: Rigid-body translation performance: (a) standard error, ρ_{px}, and (b) mean bias error, μ_{bias}, for GeoPIV and GeoPIV-RG.

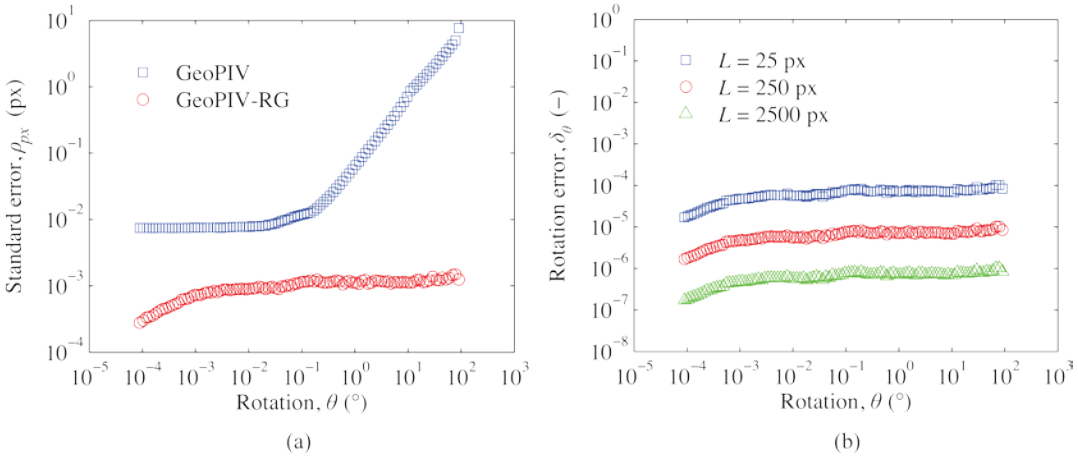

Figure 8: Rotation performance: (a) standard error for GeoPIV and GeoPIV-RG (b) effect of gauge length on rotation error, δ_θ, for GeoPIV-RG.

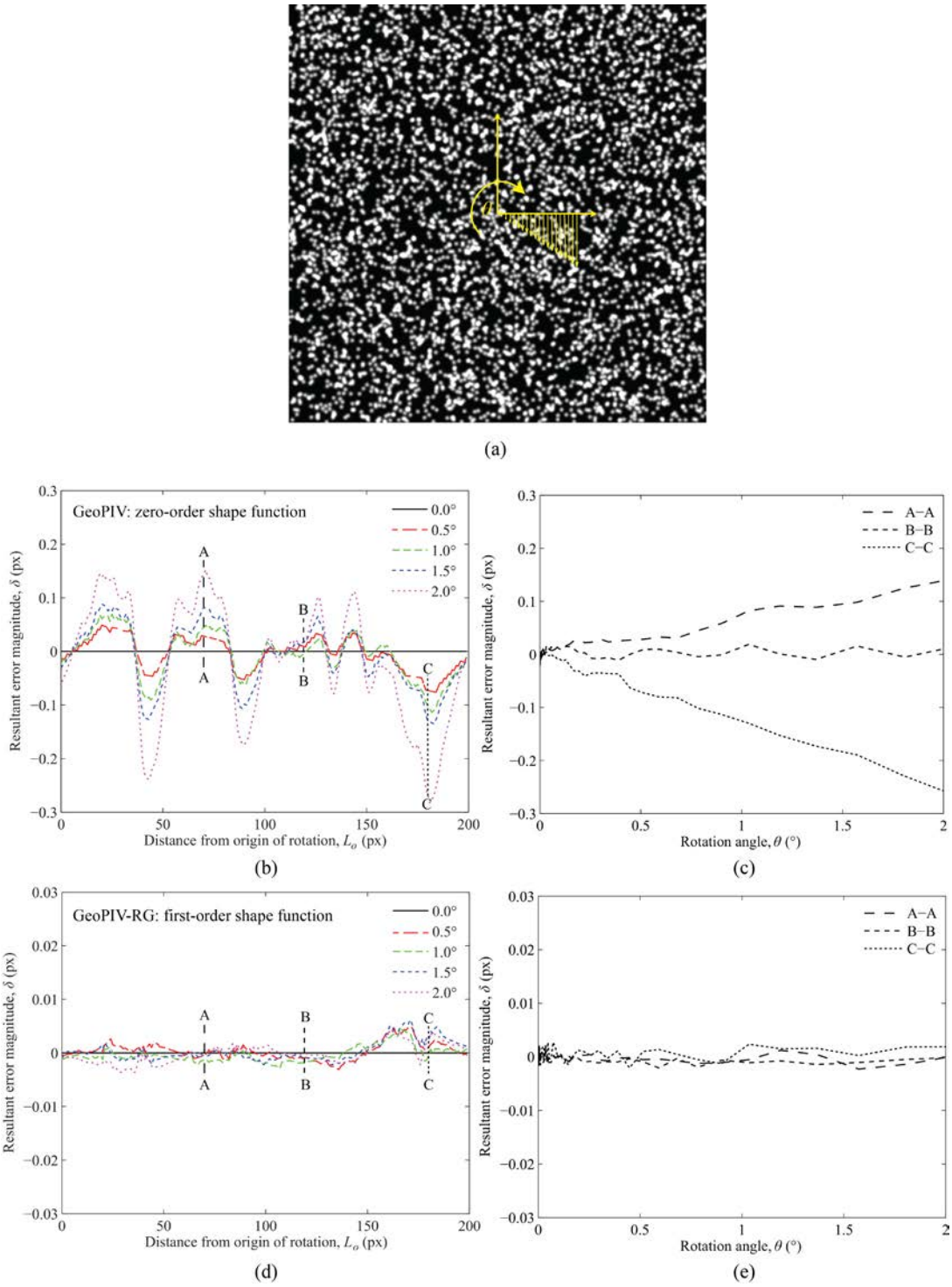

Figure 9: Randomness of rotation performance: (a) artificial image and a row of subset displacements (magnitudes amplified) illustrating the rotation imposed; (b,c) resultant error, δ_r, as a function of distance from the origin of rotation and rotation angle for GeoPIV; and (d,e) GeoPIV-RG. Note: Vertical scales are different between (a,b) and (c,d) for clarity.

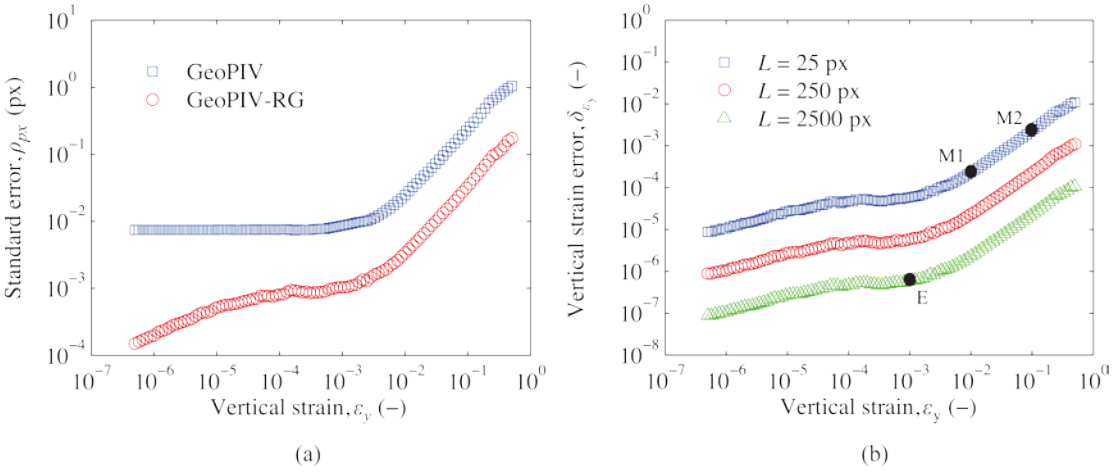

Figure 10: Vertical strain performance: (a) standard error for GeoPIV and GeoPIV-RG (b) effect of gauge length on vertical strain error, δ_{ε_y}, for GeoPIV-RG.

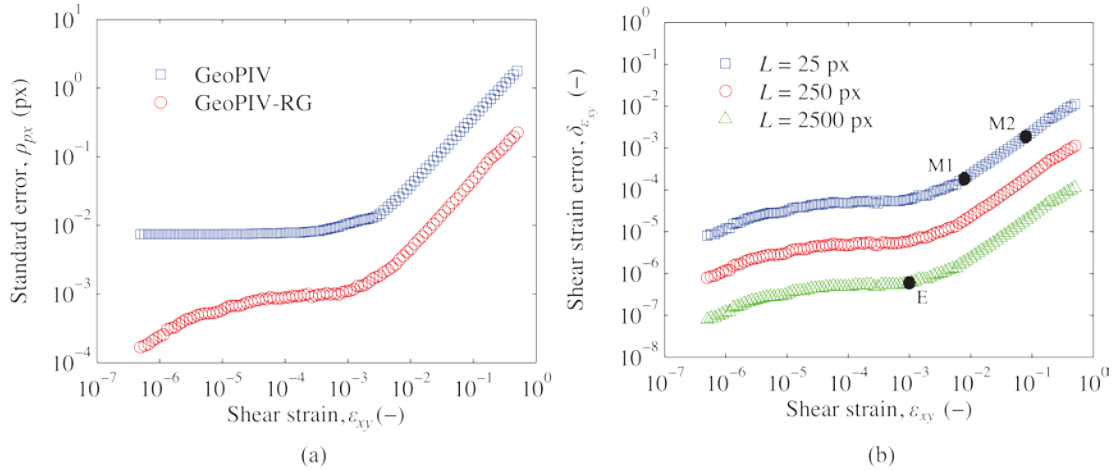

Figure 11: Shear strain performance: (a) standard error for GeoPIV and GeoPIV-RG (b) effect of gauge length on shear strain error, $\delta_{\varepsilon_{xy}}$, for GeoPIV-RG.

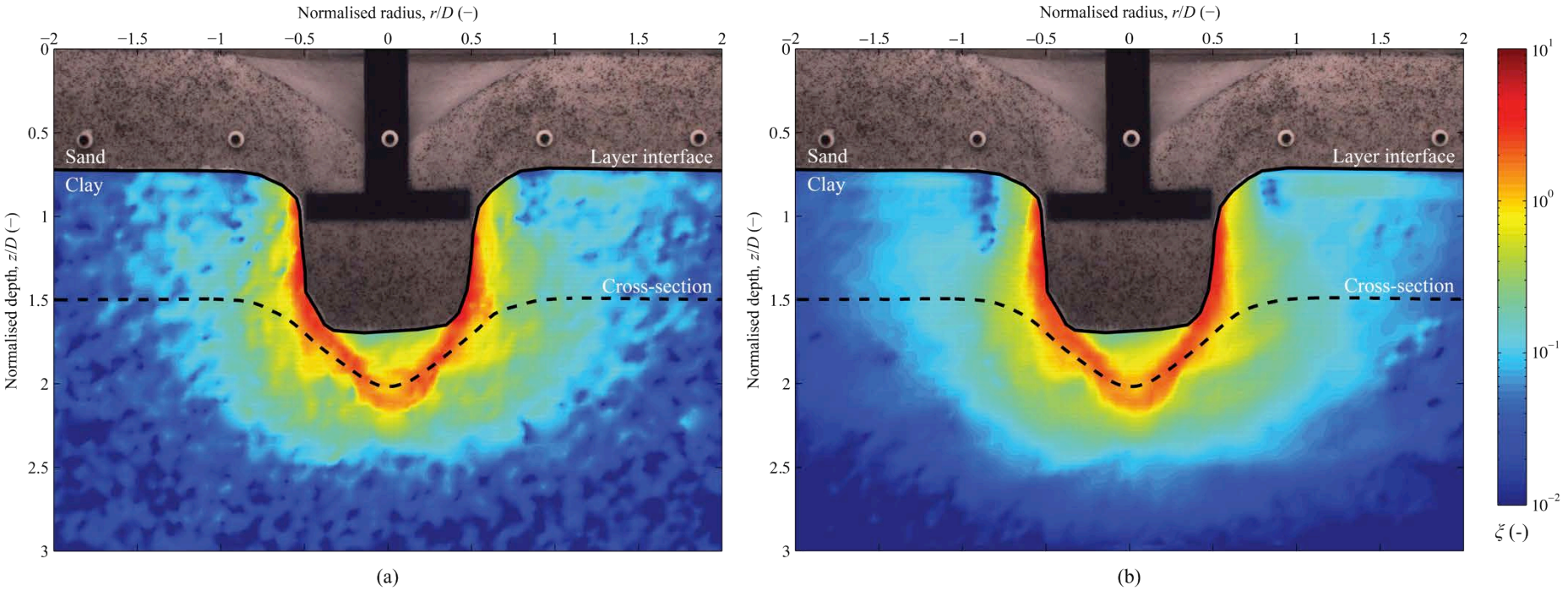

Figure 12: Example application: flat footing on sand-over-clay, total maximum shear strain ζ at 1*D* penetration using GeoPIV (a) and GeoPIV-RG (b).

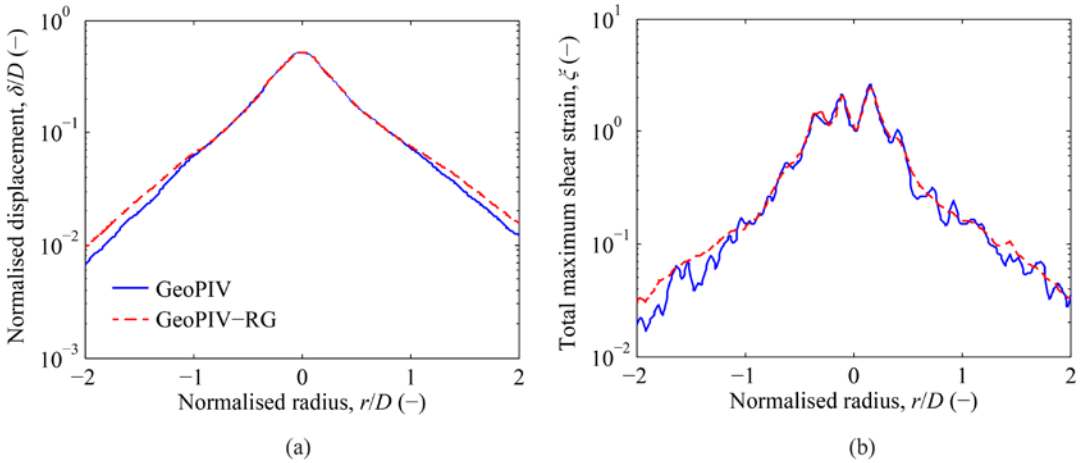

Figure 13: Normalised displacement, δ/D (a) and total maximum shear strain, ζ (b) along the cross-sections in Figures 12 (a, b) at an initial normalised depth, z/D of 1.5.

TABLES

Table 1: Computation parameters for example analysis.

GeoPIV parameters	
L_s	45px[a]
s	25px
s_{zone}	15px
Ref. image updating interval	10
GeoPIV-RG parameters	
D_s	50px[a]
s	25px
max_{iter}	50
$\|\Delta p\|_{max}$	$1x10^{-5}$
$CC_{ZNCC\text{-}seed\text{-}tol}$	0.9
$CC_{ZNCC\text{-}min\text{-}tol}$	0.75
Ref. image updating interval	~20

[a] Subset sizes chosen to have equivalent area (within ~3%).